Chem. Mater. **2004,** *16,* 3045−3055

Structure and Rheology of Hydrogen Bond Reinforced Liquid Crystals

Stephen M. Martin, Jun Yonezawa,† Matthew J. Horner,
Christopher W. Macosko, and Michael D. Ward*

*Department of Chemical Engineering and Materials Science, University of Minnesota,
421 Washington Avenue Southeast, Minneapolis, Minnesota 55455*

Received March 11, 2004. Revised Manuscript Received June 7, 2004

Phase behavior and structure in both the crystalline and liquid-crystalline states is dependent on molecular size and shape and competition between various noncovalent intermolecular interactions. Numerous guanidinium organomonosulfonate (**GS**) crystals have been shown to adopt layered architectures because of their propensity to form a two-dimensional hydrogen-bonded network consisting of the sulfonate moieties (**S**) and complementary guanidinium (**G**) ions. This characteristic has now been demonstrated for nearly all of a series of guanidinium alkylbenzenesulfonates (GCnBS), in which the alkyl chain length (n) ranges from 0 to 16 carbons, and some members of a series of guanidinium alkylbiphenylsulfonates (GCnBPS). Single-crystal X-ray diffraction reveals that these layered architectures include previously observed simple bilayer and continuously interdigitated layer architectures as well as a new “box bilayer” architecture. Whereas the related sodium organosulfonates, phenylalkanes, and biphenylalkanes alone do not form liquid-crystal phases upon heating, the reinforcement provided by the hydrogen-bonded **GS** network leads to the transformation of these crystalline phases to persistent smectic liquid-crystal phases at elevated temperatures for $n \geq$ q (as reported previously for some of the GCnBS compounds). This chain length corresponds to single-crystal packing motifs that signal the onset of a structure-directing role for alkane−alkane interactions. X-ray diffraction reveals that the d-spacings of the smectic phases increase monotonically with n, consistent with a common structure that is independent of the preexisting crystal architecture. This behavior can be ascribed to facile rearrangements of the hydrogen-bonding connectivity in the **GS** sheet during the crystal-to-smectic transition. Several GCnBS compounds also exhibit polymorphic transitions involving rearrangement of the hydrogen-bond connectivity at temperatures below the smectic transition. The general rheological behavior of the GCnBS smectic phases was consistent with that reported for other small-molecule smectics; however, the viscosity of the GCnBS smectic phases was at least 2 orders of magnitude larger. The large viscosities observed in the GCnBS smectic phases are attributed to the persistence of intermolecular hydrogen bonding in the liquid-crystal state.

Introduction

The phase behavior of liquid crystals is governed by the shape and size of their molecular constituents and a delicate balance of noncovalent intermolecular interactions.[1,2] Rod-shaped mesogens can form nematic and smectic phases, the former characterized by orientational order but an absence of the translational order observed in smectics. Disc-shaped molecules, often decorated with flexible alkyl chains, are known to form discotic columnar phases. Hydrogen bonding has been used to coerce the formation of molecular aggregates with liquid-crystal properties.[3] For example, symmetric 2:1 trimers of 4-alkoxybenzoic acid and 4,4′-bipyridyl compounds form nematic phases,[4] and dimers and trimers of uracil and diaminopyridine amphiphiles form hexagonal columnar phases.[5] Both smectic and columnar phases have been observed for amphiphilic carbohydrates and amphiphilic folic acid derivatives,[6−8] and bolaamphiphilic tetraols were reported to form lamellar mesophases.[9] The hydrogen-bond connectivity in these liquid-crystal phases, however, is difficult to surmise owing to the absence of fully characterized single-crystal

---

* To whom correspondence should be addressed. E-mail: wardx004@umn.edu.

† Asahi Kasei Corporation, 1-3-1, Yakoh, Kawasaki-ku, Kawasaki-city, Kanagawa 210-0863, Japan.

(1) Chandrasekhar, S. *Liquid Crystals*; Cambridge University Press: Cambridge, U.K., 1992.

(2) *Liquid Crystals: The Fourth State of Matter*; Saeva, F. D., Ed.; Marcel Dekker: New York, 1979.

(3) Paleos, C. M.; Tsiourvas, D. *Liq. Cryst.* **2001**, *28*, 1127.

(4) Kato, T.; Frechet, J. M. J.; Wilson, P. G.; Saito, T.; Uryu, T.; Fujishima, A.; Jin, C.; Kaneuchi, F. *Chem. Mater.* **1993**, *5*, 1094.

(5) Brienne, M. J.; Gabard, J.; Lehn, J. M.; Stibor, J. *J. Chem. Soc., Chem. Commun.* **1989**, 1868.

(6) (a) van Dorn, H. A.; van der Heijden, A. M.; de Goede, A. T. J. W.; van Rantwijk, F.; van Bekkum, H. *Liq. Cryst.* **2000**, *27*, 63. (b) Hein, M.; Miethchen, R.; Schwaebisch, D.; Schick, C. *Liq. Cryst.* **2000**, *27*, 163.

(7) Praefcke, K.; Levelut, A. M.; Kohne, B.; Eckert, A. *Liq. Cryst.* **1989**, *6*, 263.

(8) Kanie, K; Nishii, M.; Yasuda, T.; Taki, T.; Ujiie, S.; Kato, T. *J. Mater. Chem.* **2001**, *11*, 2875.

(9) Heentrich, F.; Diele, S.; Tschierske, C. *Liq. Cryst.* **1994**, *17*, 827.

10.1021/cm049594l CCC: $27.50

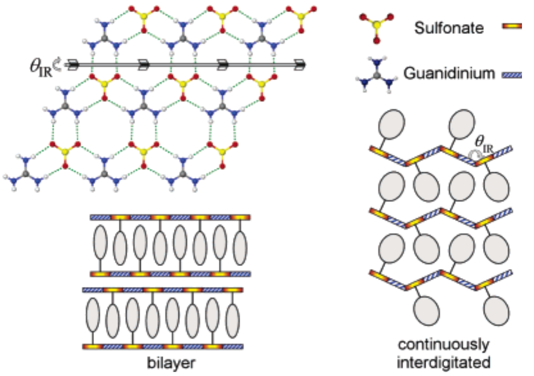

Figure 1. Schematic of the "quasihexagonal" 2-D sheet formed by the cooperative hydrogen bonding of guanidinium (**G**) and organosulfonate (**S**) ions. Schematic representations of the bilayer and continuously interdigitated layer (CIL) architectures are also depicted.

analogues. Furthermore, the effect of hydrogen bonding on the rheological properties of liquid-crystal phases has not been investigated extensively.

Recently, several reports have suggested a structural correspondence between molecular crystals and various phases of liquid crystals and block copolymers, largely as a consequence of clearly defined interfaces between dissimilar moieties.[10,11] Our laboratory has reported numerous crystalline materials with smectic-like layered architectures enforced by the presence of an infinite and well-defined two-dimensional (2-D) hydrogen-bonded network of guanidinium (**G**) ions ($C(NH_2)_3^+$) and the sulfonate (**S**) moieties of organomonosulfonates or organodisulfonates.[12−18] The 2-D network usually adopts a quasihexagonal hydrogen-bonding motif (Figure 1) due to the trigonal symmetry and chemical complementarity of the **G** and **S** ions. Two layered crystal architectures have been reported for guanidinium organomonosulfonates: the bilayer (B) architecture, in which the organic residues of the organomonosulfonates all project from the same side of the 2-D sheet and interdigitate with the organic residues of an adjacent sheet to form a discrete bilayer, and the continuously interdigitated layer (CIL) architecture, in which the organic residues project from both sides of the sheet, interdigitating to form a continuous structure. These materials are reminiscent of other layered materials, such as lamellar block copolymer microphases and smectic liquid crystals. This comparison has been extended to cylindrical phases for certain guanidinium organomonosulfonate inclusion compounds that form crystals consisting of hexagonally packed **GS** tubes.[19] Recently, guanidinium alkylbenzenesulfonates (GCnBS, $\mathbf{G}\cdot SO_3(C_6H_4)(CH_2)_{n-1}CH_3$) with even alkyl chain lengths (n) of 8 or higher were reported to form smectic liquid crystals.[20] The generic structure of these smectic phases, which exhibited d-spacings that increased monotonically with n, was surmised from the previously reported single-crystal structure of GC1BS (guanidinium tosylate),[13] which has a bilayer architecture. Single-crystal structures for the remaining GCnBS compounds, however, were not yet reported, which precluded direct examination of the relationship between single-crystal and smectic structures across the entire range of n values. Furthermore, the d-spacings assigned to GCnBS smectics for odd values of n were obtained from mixtures consisting of equal amounts of neighboring even-numbered compounds rather than pure compounds.

Herein we report the structural characterization and thermotropic properties of GCnBS compounds with alkyl chain lengths $n = 0-12$, 14, 16 and several guanidinium alkylbiphenylsulfonates (GCnBPS, $\mathbf{G}\cdot SO_3(C_{12}H_8)(CH_2)_{n-1}CH_3$; $n = 6-10$, 12, 14, 16). Single-crystal X-ray diffraction revealed various crystal architectures that reflected the delicate balance between **GS** hydrogen bonding and interactions between alkyl chains, the latter becoming more important with increasing n. Several GCnBS compounds undergo thermally driven polymorphic transitions prior to the smectic transition, which can be interpreted in terms of rearrangements of the hydrogen-bond connectivity. The apparent facility of the hydrogen-bond rearrangement may also explain the apparently common architecture for the smectic phases regardless of the initial crystal structure. The GCnBS smectic phases exhibit shear-induced yielding and shear-thinning behavior qualitatively similar to that of other small-molecule smectics. The GCnBS phases, however, exhibited viscosities that were 2 orders of magnitude greater than typical small-molecule smectic phases, a characteristic that can be attributed to reinforcement by **GS** hydrogen bonding.

Results and Discussion

Structures of Crystalline GCnBS and GCnBPS Compounds. Guanidinium organomonosulfonates show a pronounced tendency to crystallize in layered structures due to the persistent sheetlike network formed by complementary hydrogen bonding between guanidinium (**G**) ions and the sulfonate (**S**) moiety of the organomonosulfonate (Figure 1). The 2-D **GS** sheet can be described as a series of hydrogen-bonded **GS** ribbons fused by hydrogen bonding along adjoining edges. The sheets in many **GS** compounds exhibit puckering about these edges to accommodate close packing of the organic residues ($\theta_{IR} = 180°$ for a perfectly flat sheet). Bilayer architectures are naturally limited to $\theta_{IR} = 180°$. The sheets in CIL architectures, however, can become highly puckered, with θ_{IR} values as low as 73° having been observed (see below).

Fully refined single-crystal structures for GCnBS with $n = 2$, 3, 4, 7, 11, 12, 14, and 16 are reported here (Tables 1 and 2). The crystal quality for $n = 5$, 6, and 10 was rather poor, permitting only partial refinements

---

(10) Xu, Z.; Kiang, Y.-H.; Lee, S.; Lobkovsky, E. B.; Emmott, N. *J. Am. Chem. Soc.* **2000**, *122*, 8376.

(11) Horner, M. J.; Holman, K. T.; Ward, M. D. *Angew. Chem., Int. Ed.* **2001**, *40*, 4045.

(12) Russell, V. A.; Etter, M. C.; Ward, M. D. *Chem. Mater.* **1994**, *6*, 1206.

(13) Russell, V. A.; Etter, M. C.; Ward, M. D. *J. Am. Chem. Soc.* **1994**, *116*, 1941.

(14) Russell, V. A.; Ward, M. D. *J. Mater. Chem.* **1997**, *7*, 1123.

(15) Russell, V. A.; Evans, C. C.; Li, W.; Ward, M. D. *Science (Washington, D.C.)* **1997**, *276*, 575.

(16) Holman, K. T.; Ward, M. D. *Angew. Chem., Int. Ed.* **2000**, *39*, 1653.

(17) Holman, K. T.; Martin, S. M.; Parker, D. P.; Ward, M. D. *J. Am. Chem. Soc.* **2001**, *123*, 4421.

(18) Holman, K. T.; Pivovar, A. M.; Swift, J. A.; Ward, M. D. *Acc. Chem. Res.* **2001**, *34*, 107.

(19) Horner, M. J.; Holman, K. T.; Ward, M. D. *Angew. Chem., Int. Ed.* **2001**, *40*, 4045.

(20) Mathevet, F.; Masson, P.; Nicoud, J.-F.; Skoulios, A. *Chem.—Eur. J.* **2002**, *8*, 2248.

Table 1. Crystallographic Information and Selected Structural Features for GC2BS, GC3BS, GC4BS, GC7BS, and GC11BS

compound	GC2BS	GC3BS	GC4BS	GC7BS	GC11BS
formula	$C_9H_{15}N_3O_3S$	$C_{10}H_{17}N_3O_3S$	$C_{11}H_{19}N_3O_3S$	$C_{14}H_{25}N_3O_3S$	$C_{18}H_{33}N_3O_3S$
formula wt.	254.33	259.30	273.35	315.43	363.47
cryst. syst.	orthorhombic	orthorhombic	orthorhombic	orthorhombic	triclinic
space group	ama2	Pnma	Pnma	$P2_12_12_1$	P-1
color	clear	clear	clear	clear	clear
a (Å)	7.437(1)	22.130(2)	24.773(2)	7.1549(7)	7.796(2)
b (Å)	21.845(4)	7.5101(8)	7.5708(6)	11.9854(12)	11.825(4)
c (Å)	7.223(1)	7.6858(8)	22.3375(19)	20.579(2)	23.588(7)
α (deg)	90	90	90	90	82.830(5)
β (deg)	90	90	90	90	86.091(5)
γ (deg)	90	90	90	90	89.365(5)
V (Å^3)	1173.4	1277.4(2)	4189.5(6)	1764.7(3)	2152.6(11)
temp (K)	*173(2)*	*173(2)*	*173(2)*	*173(2)*	*173(2)*
Z	2	4	12	4	4
R_1 [$I>2s(I)$]	0.0248	0.0655	0.0645	0.0650	0.0664
wR_2 [$I>2s(I)$]	0.0664	0.1949	0.1418	0.1413	0.1656
G.O.F.	1.066	1.396	1.010	0.896	0.996
θ_{IR} (deg)	72.67	80.13	73.90	128.49	180.00
architecture	CIL	CIL	CIL	CIL	B
d-spacing	10.92	11.07	12.39	10.29	23.35

Table 2. Crystallographic Information and Selected Structural Features for GC12BS, GC14BS, GC16BS, GC8BPS, and GC10BPS

compound	GC12BS	GC14BS	GC16BS	GC8BPS	GC10BPS
formula	$C_{19}H_{35}N_3O_3S$	$C_{21}H_{39}N_3O_3S$	$C_{23}H_{43}N_3O_3S$	$C_{21}H_{31}N_3O_3S$	$C_{21}H_{31}N_3O_3S$
formula wt.	385.56	413.61	441.66	405.56	433.69
cryst. syst.	monoclinic	monoclinic	monoclinic	orthorhombic	monoclinic
space group	$P2_1/n$	$P2_1/c$	$P2_1/c$	$P2_12_12_1$	$P2_1/c$
color	clear	clear	clear	clear	clear
a (Å)	7.909(2)	7.8868(8)	7.9138(3)	7.619(1)	7.669(2)
b (Å)	10.180(2)	10.1325(10)	10.1427(4)	7.710(1)	7.924(2)
c (Å)	54.54(1)	59.017(6)	63.907(2)	36.330(6)	38.321(8)
α (deg)	90.00	90	90	90	90
β (deg)	93.94(3)	92.131(2)	90.032(2)	90.00	92.893(3)
γ (deg)	90.00	90	90	90	90
V (Å^3)	4381(2)	4713.0(8)	5129.6(3)	2134.0	2325.7(8)
temp (K)	*173(2)*	*173(2)*	*173(2)*	*173(2)*	*173(2)*
Z	8	8	8	4	4
R_1 [$I > 2s(I)$]	0.1411	0.0983	0.0983	.0327	.1114
wR_2 [$I > 2s(I)$]	0.3467	0.2464	0.2495	0.0840	0.2236
G. O. F.	1.245	1.300	1.193	1.069	1.130
θ_{IR} (deg)	n/a	n/a	n/a	81.87	85.09
architecture	BB	BB	BB	CIL	CIL
d-spacing (Å)	27.21	29.49	31.95	18.17	19.14

of single-crystal data. Nonetheless, these data were sufficient to determined unit-cell parameters and deduce the general features of molecular packing and the puckering angles. Some of these compounds ($n = 8, 9$) did not form crystals of sufficient quality for single-crystal X-ray diffraction despite numerous attempts at crystallization in various solvents. Furthermore, polymorphs obtained upon heating some of these compounds (see below) could not be obtained in single-crystal form. In these cases Fourier transform infrared spectroscopy (FTIR) and powder X-ray diffraction (PXRD) proved useful in establishing the hydrogen-bond connectivity in the **GS** sheet, crystal architectures, and d-spacings.

Earlier single-crystal X-ray diffraction studies performed in our laboratory demonstrated that GC0BS (guanidinium benzenesulfonate) and GC1BS (guanidinium tosylate) adopted bilayer architectures.[12,13] In contrast, highly puckered CIL architectures ($\theta_{IR} < 90°$), in which the alkyl chains adopt all-*trans* conformations, were observed for $n = 2-6$, as exemplified here for GC3BS (Figure 2).[21] The organic residues of opposing **GS** sheets interdigitate such that the alkyl chains overlap phenyl groups on the opposing **GS** sheet. GC7BS also adopted a CIL architecture, but the alkyl chains exhibited a single gauche conformation about the $C_\alpha-C_\beta$ bond (herein denoted as the $\text{CIL}_{\text{gauche}}$ architecture), resulting in parallel alignment of the alkyl chains with the **GS** sheet. Consequently, this compound has a smaller interlayer d-spacing ($d = 10.29$ Å) compared with GC6BS ($d = 13.78$ Å). The longer "footprint" of the alkyl chains on the **GS** sheet results in a larger θ_{IR} value (i.e., less puckering) than any of the compounds with the $\text{CIL}_{\text{all}-trans}$ architecture. The gauche conformation, which is slightly less preferred than all-trans in alkanes,[17] suggests the C7 alkyl chains are sufficiently long for alkyl−alkyl interactions to overcome the energetic penalty of the gauche conformation. Although the **GS** sheet is maintained, this dramatic change in the organization of the aliphatic chains suggests a threshold at which interchain interactions begin to play a more significant role in crystal packing. Notably, GC7BS is the first compound in this series to form a smectic phase (isotropic melts were observed for $n = 0-6$, see below). Because the **GS** sheet is common to all these compounds, this behavior appears to signal the onset of structure-directing interchain interactions.

---

(21) Remarkably, GC2BS adopts a CIL structure but also crystallizes in polar space group *ama2* in an arrangement similar to that reported for certain guanidinium disulfonates with 'bent' pillars.[18]

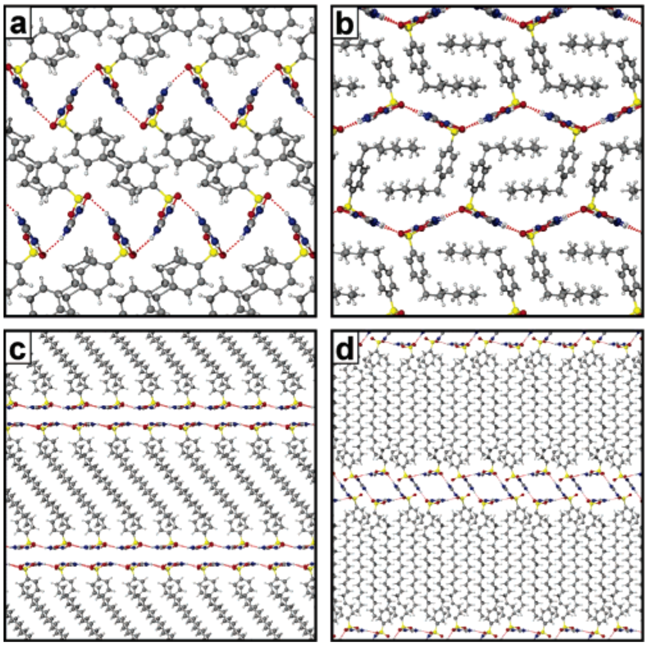

Figure 2. Crystal structures of (a) GC3BS, (b) GC7BS, (c) GC11BS, and (d) GC14BS which adopt $\mathrm{CIL}_{\text{all}-trans}$, $\mathrm{CIL}_{\text{gauche}}$, bilayer, and box bilayer (BB) architectures, respectively, as determined by single-crystal X-ray diffraction (see Table 1).

In the case of GC10BS, the partially refined single-crystal data allowed determination of unit-cell parameters, the positions of the **G** ions and phenylsulfonate moieties, and the puckering angle, whereas for GC8BS and GC9BS only the interlayer *d*-spacings were available from PXRD measurements. The diffraction patterns for GC7BS−GC10BS are essentially identical except for the expected small shifts in 2θ, and the interlayer *d*-spacings and the puckering angles for C7−C10 increase linearly with n.[22] This signifies a common CIL architecture with $C_\alpha-C_\beta$ gauche conformations in the alkyl chains. Furthermore, FTIR spectra of these compounds in the $\nu_{\mathrm{N-H}}$ region (see below) were identical to those for $n = 2$, 3, 4, and 7, confirming the presence of the quasihexagonal **GS** sheet motif expected for the CIL architecture.

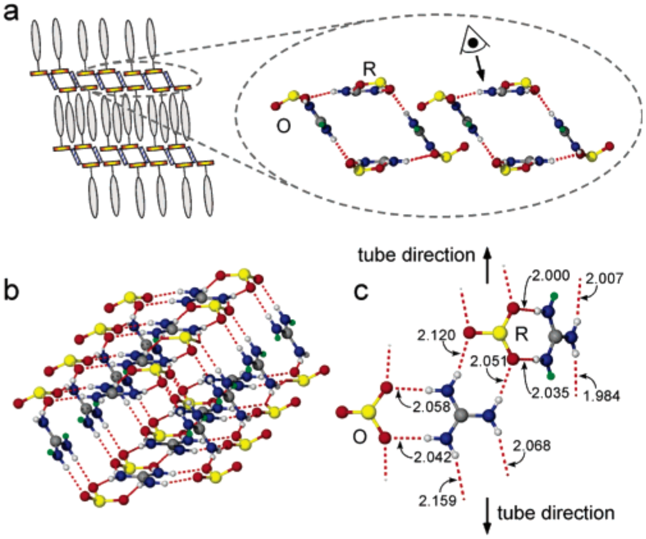

Figure 3. (a) Schematic representation of the box bilayer architecture in GC12BS, GC14BS, and GC16BS. Each hydrogen-bonded ‘tube’ consists of two **GS** ribbons formed by hydrogen bonding between **G** ions and intraribbon sulfonates (denoted as “R”), joined by perpendicular **G** ions (the organic residues of the organomonosulfonates are omitted for clarity). The tubes also form hydrogen bonds with outlying **S** ions in neighboring ribbons (denoted as “O”). (b) The structure of a single tube. (c) The hydrogen-bond motif as viewed from above the tube (see panel a). The perpendicular **G** ion at the right projects into the plane of the page to connect to the opposing ribbon. The hydrogen atoms shaded green are not involved in hydrogen bonding. Bond distances are in Angstroms.

In contrast to $n = 2-10$, GC11BS reverted to the bilayer architecture observed for GC0BS and GC1BS, with the alkyl chains adopting an all-*trans* configuration. This probably reflects an alkyl chain with a footprint that surpasses the metric limits of the **GS** sheet, thereby prohibiting formation of the $\mathrm{CIL}_{\text{gauche}}$ architecture with the chains parallel to the sheet. Surprisingly, GC12BS, GC14BS, and GC16BS exhibited a layered architecture that has not been observed previously (Figure 2d). The new architecture, dubbed *box bilayer* (BB), differs substantially from the quasihexagonal motif, with one-half of the **G** ions oriented parallel to the bilayers but the other half nearly perpendicular to the bilayers (Figure 3). The obvious structural elements of this architecture are 1-D hydrogen-bonded **GS** tubes oriented along the *a*-axis that link adjacent bilayers, each tube consisting of two opposing **GS** ribbons connected by perpendicular **G** ions (Figure 3). The tubes also form hydrogen bonds with outlying **S** ions in neighboring ribbons (denoted as “O” in Figure 3). Only four of the protons on each perpendicular **G** ion participate in hydrogen bonding with the ribbons. The distance between the two unassociated N−H protons (highlighted green in Figure 3) and the nearest **S** oxygen was 2.57 Å, beyond the value expected for hydrogen bonding. The FTIR spectra for compounds with the BB architecture confirmed the presence of unassociated N−H protons (see below). These structural features reveal that the **GS** sheet in the BB architecture is discontinuous, implying that the layered architecture is driven by the dispersive interactions between the long alkyl chains projecting from the **GS** ribbons. The departure from the quasihexagonal **GS** motif can be explained by the increasingly important role of interchain forces as the alkyl chain length is increased. Assuming a cross-sectional area of 21 Å^2 for a single alkyl chain, close packing of a pair of interdigitated alkyl substituents requires an area of 42 Å^2 on each **GS** sheet, which is somewhat less the area of 45 Å^2 available for that pair on a planar quasihexagonal **GS** sheet in the bilayer architecture (Figure 4). Furthermore, the 42 Å^2 area is much less than the 90 Å^2 available for the interdigitated pair on a flat **GS** sheet in the CIL architecture. Even the most highly puckered **GS** sheet observed ($\theta_{\mathrm{IR}} = 72°$) has 54 Å^2 available for an interdigitated pair. Consequently, interdigitation of vertically oriented alkyl chains in the bilayer and CIL architectures will always be accompanied by void space that would frustrate close packing. The BB architecture, however, provides an avenue to close packing of vertically aligned alkyl chains by expelling a guanidinium ion out of the plane of the **GS** sheet.

---

[22] Room-temperature PXRD *d*-spacings: GC7BS (10.6 Å), GC8BS (11.0 Å), GC9BS (11.2 Å), GC10BS (11.5 Å). θ_{IR}: GC7BS (128.5°), GC10BS (154.3°).

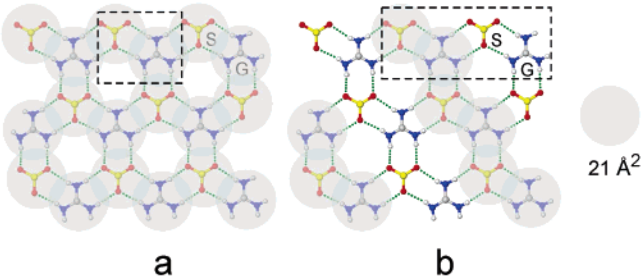

Figure 4. Schematic representation of footprints of alkyl chains projected onto flat GS sheets in (a) bilayer and (b) CIL architectures.

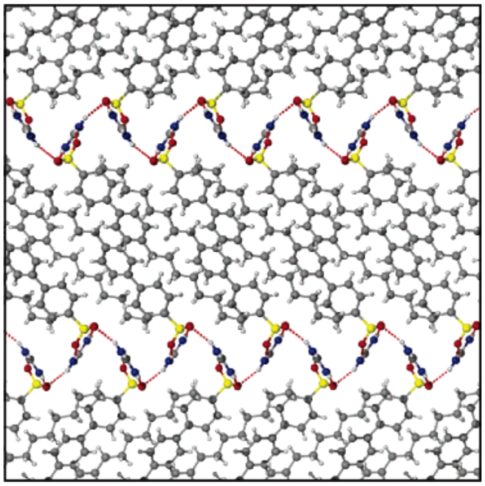

Figure 5. Crystal structure of GC8BPS, which adopts the CIL architecture, as determined by single-crystal X-ray diffraction (see Table 1).

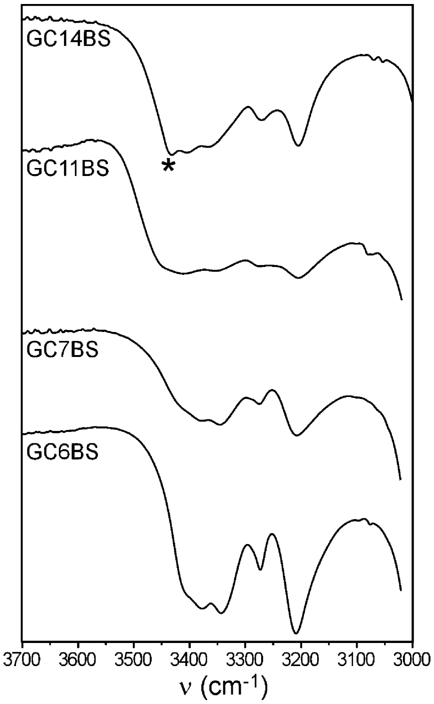

Figure 6. FTIR spectra of GC6BS, GC7BS, GC11BS, and GC14BS in the ν_{N-H} region. The N−H groups not involved in hydrogen bonding in GC14BS produce an extra ν_{N-H} mode at 3430 cm^{-1} (denoted by an asterisk) compared with the quasihexagonal hydrogen-bonding motif of the other structures.

Single-crystal X-ray structures for the guanidinium biphenylsulfonates GC1BPS, GC2BPS, and GC6BPS were reported previously by our laboratory,[23] and the crystal structures of GC8BPS and GC10BPS are provided here (Figure 5). GC1BPS and GC2BPS adopt bilayer crystal architectures, with the **GS** sheet adopting a quasihexagonal hydrogen-bonding motif in GC1BPS but a shifted-ribbon hydrogen-bond motif in GC2BPS, wherein the 1D **GS** ribbons are shifted with respect to each other along the ribbon axis. Unlike previously reported shifted-ribbon motifs,[24] the shift ribbon in GC2BPS retains the maximum number of hydrogen bonds. GC6BPS, GC8BPS, and GC10BPS all form highly puckered CIL architectures in which the alkyl chains adopt all-*trans* configurations, with interlayer *d*-spacings that increase monotonically with chain length (d_{C6} = 16.72 Å; d_{C8} = 18.16 Å; d_{C10} = 19.14 Å). The crystal structures of other compounds in the GCnBPS series were not determined because high-quality single crystals could not be obtained even after numerous attempts. The interlayer *d*-spacings for GC12BPS (d_{C12} = 27.17 Å) and GC14BPS (d_{C14} = 27.43 Å) deduced from PXRD, however, were much larger than expected based on the increased chain length alone, suggesting a different architecture. Although the FTIR spectra of these compounds indicated a quasihexagonal GS sheet for all these compounds, the absence of a single-crystal structure made the assignment of a specific architecture impossible.

Thermal Behavior. Differential scanning calorimetry of the GCnBS compounds with $n \geq 11$ revealed phase transitions to other crystalline polymorphs at temperatures well below the transitions to their corresponding smectic phases (see below). The transition temperatures between crystalline forms ($T_{C1\rightarrow C2}$) increased with the length of the alkyl substituent (C11 = 86.6°; C12 = 89.3°; C14 = 95.3°; C16 = 131.3°). These transitions were irreversible. The polymorphic transitions for GC11BS, GC12BS, GC14BS, and GC16BS were corroborated by temperature-dependent FTIR spectroscopy and PXRD. Previous studies have demonstrated that guanidinium ν_{N-H} stretching modes occurring in the spectral range 3000−3700 cm^{-1} are diagnostic of the **GS** hydrogen-bonding motif.[24] Hydrogen bonding shifts the ν_{N-H} peaks to lower energy, with the quasihexagonal **GS** motif typically associated with two higher energy ν_{N-H} peaks in this group. For example, GC11BS (bilayer architecture) exhibited ν_{N-H} = 3345 and 3404 cm^{-1} and GC6BS and GC7BS (CIL architecture) exhibited ν_{N-H} = 3332 and 3367 cm^{-1} (Figure 6). In contrast, GC14BS, with the BB architecture, exhibited three peaks at ν_{N-H} = 3365, 3403, and 3430 cm^{-1}. The higher energy ν_{N-H} mode at 3430 cm^{-1} can be attributed to the guanidinium N−H groups not involved in hydrogen bonding. These distinguishing spectral features permitted assignment of the hydrogen-bond motif during phase transformations.

The ν_{N-H} peaks of GC7BS at 3332 and 3367 cm^{-1} (Figure 7a) broadened when heated to 220 °C (above

---

[23] Plaut, D. J.; Martin, S. M.; Kjaer, K.; Weygand, M. J.; Lahav, M.; Leiserowitz, L.; Weissbuch, I.; Ward, M. D. *J. Am. Chem. Soc.* **2003**, *125*, 15922.

[24] Russell, V. A. *Hydrogen Bonding and Control of Molecular Packing in the Organic Solid State with Implications for Materials Design*; Ph.D. Thesis, Department of Chemistry, University of Minnesota: Minneapolis, 1995; p 271.

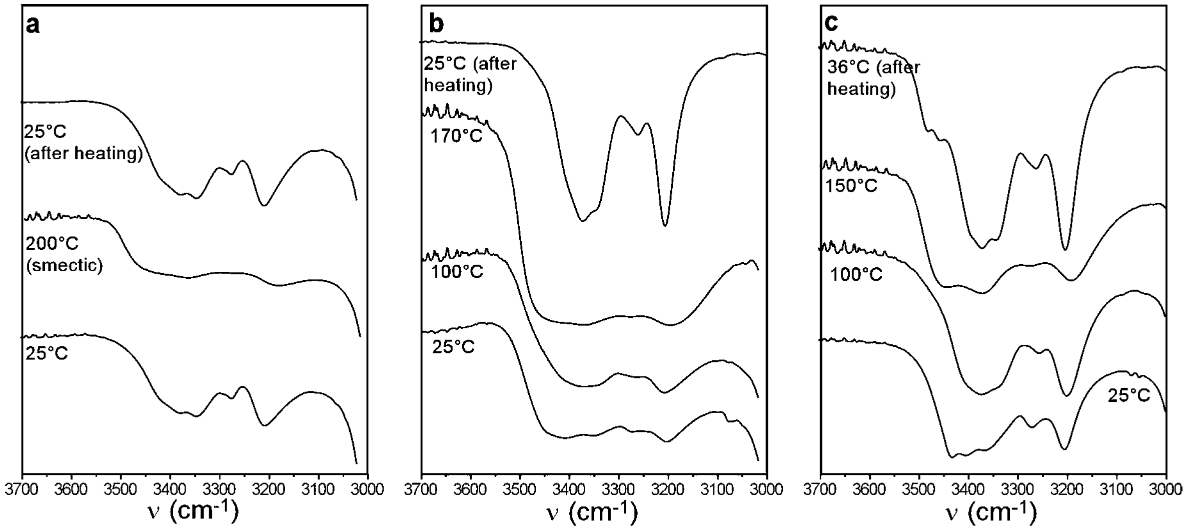

Figure 7. IR spectra of (a) GC7BS, (b) GC11BS, and (c) GC14BS in the N−H stretching region. Note that the GC11BS and GC14BS spectra change upon heating and cooling, indicating a shift in the **GS** hydrogen-bonding motif.

the smectic transition; see below) and reappeared upon cooling. Similar behavior was observed for GC8BS, GC9BS, and GC10BS. The spectrum of GC11BS at 100 °C, however, exhibited only a single, broad $\nu_{\mathrm{N-H}}$ peak at 3362 cm $^{-1}$, revealing a different hydrogen-bonding motif than at 25 °C. Above the smectic transition at $T_{\mathrm{C\rightarrow S}} = 140$ °C, this peak broadened noticeably, but unlike the previous compounds, the original $\nu_{\mathrm{N-H}}$ peaks at 3345 cm $^{-1}$ and 3404 cm $^{-1}$ did not reappear upon cooling to 25 °C. Instead, two $\nu_{\mathrm{N-H}}$ peaks were observed at 3342 and 3370 cm $^{-1}$, signifying a structure different than that observed before thermal cycling. The spectrum of GC14BS (Figure 7c) at 100 °C exhibited a single broad $\nu_{\mathrm{N-H}}$ peak at 3371 cm $^{-1}$, similar to that observed for GC11BS, and two broad peaks were apparent above $T_{\mathrm{C\rightarrow S}} = 121$ °C. After cooling, this compound exhibited $\nu_{\mathrm{N-H}} = 3342$ and 3370 cm^{-1}, substantially different than its original values but essentially identical to those for the transformed GC11BS. The absence of the third $\nu_{\mathrm{N-H}}$ peak at 3430 cm $^{-1}$ in the transformed GC14BS suggests that all of the guanidinium N−H groups in the new polymorph participate in hydrogen bonding, consistent with the disappearance of the BB architecture and the likely formation of a bilayer or CIL architecture.

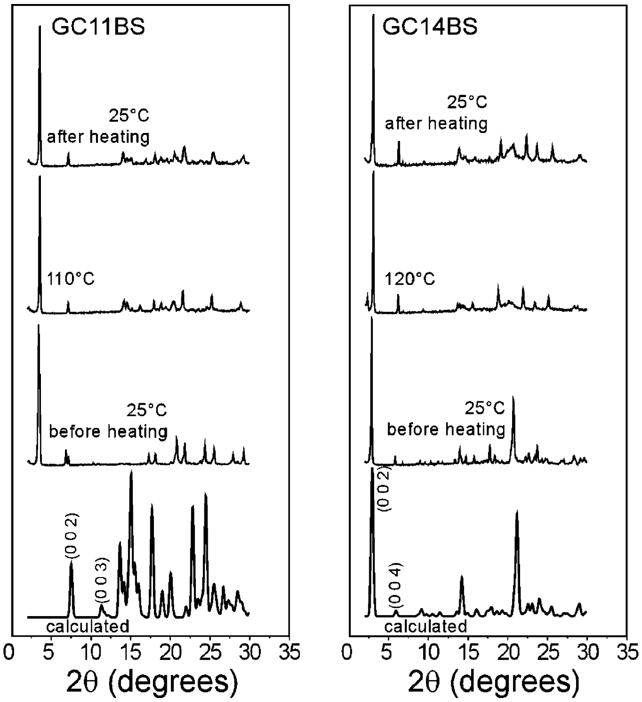

Figure 8. Powder XRD patterns for GC11BS and GC14BS taken at various temperatures. The appearance of new peaks and shifts of other peaks indicate irreversible structural changes upon heating. The patterns in the bottom panels were calculated from the single-crystal structures in Table 1. Although the Miller index assignments for the crystalline phases are fully characterized from the single-crystal data, only the (00l) peaks are labeled in the calculated pattern as they correspond to the diffraction peaks that are characteristic of their smectic phases.

PXRD measurements performed in parallel with the FTIR measurements revealed that the diffraction patterns for GC7BS measured at 25 and 150 °C were almost identical, substantiating the absence of a phase transition for this material. The PXRD data agreed well with the pattern calculated from single-crystal structure data acquired at −100 °C. The interlayer d-spacings deduced from the diffraction patterns of GC10BS at 25 and 155 °C were consistent with those calculated from single-crystal X-ray diffraction at −100 °C. The intense peak at $2\theta = 20.7°$ recorded at room temperature (25 °C) shifted slightly to $2\theta = 20.1°$ when the compound was heated to 155 °C. This shift was reversible upon cooling and, therefore, could be attributed simply to thermal expansion. In contrast, the PXRD diffraction pattern of GC11BS differed substantially from the pattern calculated from its single-crystal structure even before heating, with the peak at $2\theta = 3.45°$ corresponding to d_{001} conspicuously absent (Figure 8a). This suggests that grinding of GC11BS during sample preparation for PXRD measurements induced a phase transformation to a polymorphic form. Upon heating this material to 110 °C a third polymorph was evident from the PXRD data; this crystal form did not revert to either of the original low-temperature structures upon cooling, corroborating the irreversibility deduced from the FTIR measurements.

The diffraction pattern for GC14BS, which at 25 °C agrees with the pattern calculated from single-crystal data (Figure 8b), changed significantly upon heating.

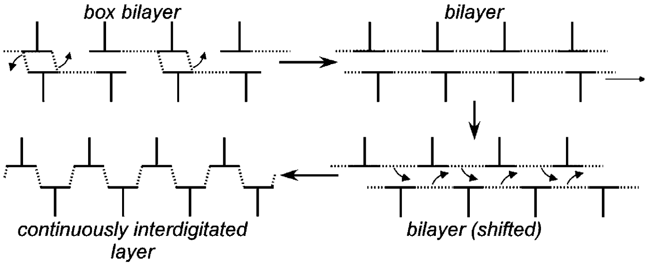

Figure 9. Schematic of the mechanism for the polymorphic transition from the box bilayer architecture to the quasihexagonal bilayer or CIL architectures. Guanidinium hydrogen-bond linkages are denoted as dotted lines between the (solid) sulfonates. The **G** linkages are 'pushed' from one sulfonate to another to produce the new polymorphs.

The (004) peak shifted from $2\theta = 5.85°$ at 25 °C ($d_{004} = 15.09$ Å) to $2\theta = 6.2°$ at 120 °C ($d_{004} = 14.24$ Å). The intense peak at $2\theta = 20.75°$ at 25 °C, assignable to the (12−3) reflection based on the single-crystal structure (Table 1), virtually disappeared at 120 °C, with new peaks emerging at $2\theta = 18.8°$ and 21.95°. This new form was maintained upon cooling. PXRD data for GC12BS and GC16BS revealed similar polymorphic behavior, indicating that the BB polymorphs are *metastable* and readily transform to more stable modifications upon heating. The apparent metastability of the BB polymorphs may be due to the void space (48 Å^3 per unit cell) that exists in the interior of the **GS** tubes bridging adjacent bilayers. It is important to note that the overall intensities of the diffraction peaks did not decrease appreciably during these transformations, indicating that the changes in the diffraction pattern were not associated with a loss of crystallinity. The PXRD patterns and DSC scans of GC12BPS and GC14BPS indicated a transition to another polymorph upon heating above ca. 76 °C. The formation of these new phases was irreversible and characterized by a significant increase in the interlayer d-spacing, for example, from $d = 28.3$ to 31.0 Å in the case of GC12BPS. The FTIR spectra of GC12BPS and GC14BPS indicated that the quasihexagonal **GS** motif was maintained in the new polymorph.

The facile phase transformations between layer architectures in these GCnBS compounds suggests a pathway by which the **G···S** hydrogen-bond connectivity can change without severe disruption of the stratified layers. Indeed, slight motions of the out-of-plane guanidinium ions in the BB architecture, accompanied by a small amount of translation of the layers, would allow formation of the bilayer architecture (Figure 9) or the CIL architecture (not shown) with the quasihexagonal **GS** motif. Related motions of the guanidinium ions also would allow interconversion of the bilayer and CIL architectures, with minimal motions of the organosulfonates. The ease of these transformations also explains the formation of a common smectic architecture that is independent of the starting crystal phase. Optical microscopy of GCnBS single crystals indicates that these phase changes are not single-crystal to single-crystal transitions, as the crystals fractured and became opaque when they were heated through their polymorphic transition temperatures.

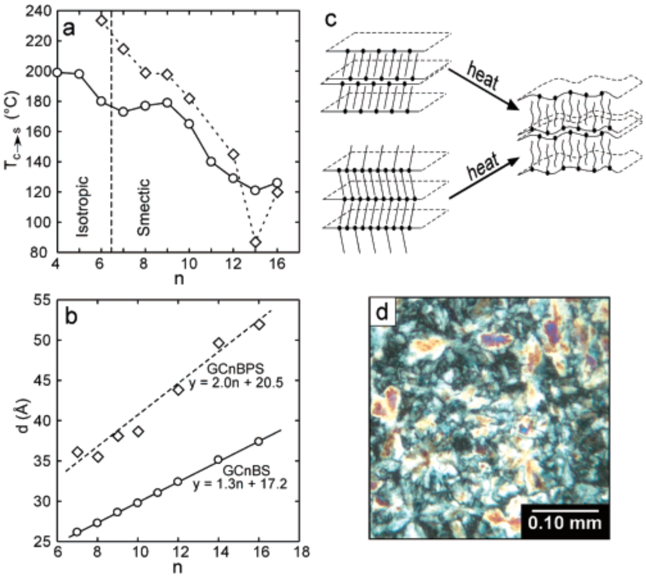

Figure 10. (a) Isotropic melting and smectic transition temperatures for GCnBS (○) and GCnBPS (◇). (b) Characteristic interlayer d-spacings for the smectic phases of GCnBS (○) and GCnBPS (◇). (c) Schematic depicting the smectic transition from a layered molecular crystal (either a bilayer or CIL architecture) to a smectic liquid-crystal phase upon heating. (Inset) Polarized optical microscope image of the smectic phase of GC8BS at 220 °C.

GCnBS and GCnBPS Liquid-Crystalline Phases. The layered crystal architectures adopted by GCnBS compounds can be viewed as mimics of lamellar morphologies observed in softer materials such as block copolymers and smectic liquid crystals. The organization of **GS** compounds into structures consisting of alternating layers of polar groups (**G** and **S**) and nonpolar organic residues is enforced by the persistent 2-D hydrogen-bonded **GS** network. Recently, Mathevet et al. reported that crystalline GC8BS, GC10BS, GC12BS, and GC14BS, for which single-crystal structures were not yet available, transformed to smectic liquid-crystal phases upon heating, whereas GC6BS formed an isotropic melt.[20] On basis of examination of the melting behavior of mixtures of even-numbered GC6BS and GC8BS, the threshold for smectic phase formation was deduced to be $n = 6.8$. Direct measurements of the properties of $n =$ odd compounds, including GC7BS, were not reported. The isotropic melting temperatures ($T_{C\rightarrow I}$), smectic transition temperatures ($T_{C\rightarrow S}$), and characteristic interlayer spacings (d) of the GCnBS smectic phases are displayed in Figure 10. These measurements, which relied on pure compounds with $n =$ odd, including $n = 7$ (i.e., not mixtures), demonstrate clearly that the crossover from isotropic melt to smectic phase occurs between $n = 6$ and 7 carbons. We observed, however, that minute amounts of impurity, such as phenylheptane, can inhibit formation of the GC7BS smectic phase or lower its $T_{C\rightarrow S}$. Parallel studies of the phase behavior of phenylalkanes and sodium alkylbenzenesulfonates demonstrated that neither of these materials exhibited smectic liquid-crystal behavior, indicating that hydrogen bonding between the **G** and **S** ions is necessary for the formation of smectic phases.

The characteristic smectic d-spacings were substantially larger than those of their corresponding crystalline phases, although it is notable that the smectic d-spacings most closely resemble the values for the

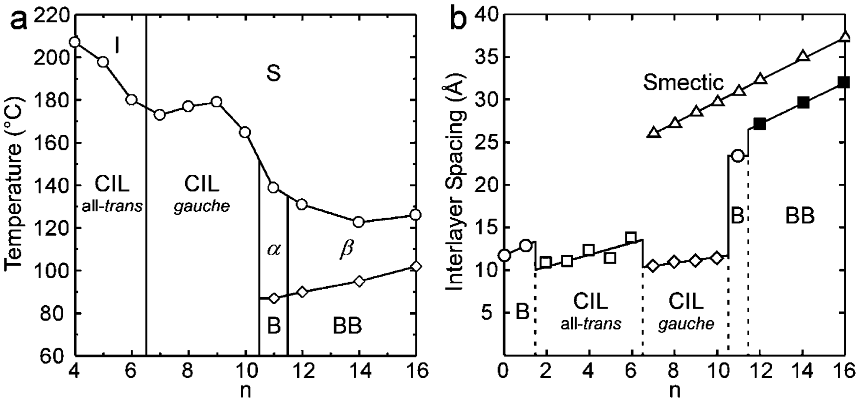

Figure 11. (a) Phase diagram of the GCnBS system denoting the **GS** architecture of the crystalline phase and the isotropic and smectic phases with respect to alkyl chain length *n* and temperature. (b) Characteristic interlayer spacings the GCnBS crystalline architectures (○, bilayer; □, all-*trans* continuously interdigitated layer; ◇, gauche CIL; ■, box bilayer) and the GCnBS smectic phases (△).

materials with the BB architecture. The smectic *d*-spacings increased linearly with alkyl chain length as expected, with no apparent odd−even effects. The nearly perfect linear dependence indicated that these smectic phases shared a common architecture despite the different architectures of their single-crystal phases prior to $T_{\mathrm{C}\rightarrow\mathrm{S}}$. The slope of the GCnBS data, $m = 1.3$, is very near the value of 1.2 Å expected based on the projected length of a methylene unit along an all-*trans* chain. This would appear to suggest these materials can be described as smectic A phases, although smectic C with a slight chain tilt cannot be ruled out entirely, particularly if the *d* spacing is prone to expansion by adventitious phenylalkane impurities. The optical micrographs, which reveal conical fan structures, were not conclusive with respect to distinguishing between smectic A and C. The *d*-spacings of the smectic phases also were independent of the thermal history of the materials. In the cases of GC11BS, GC12BS, GC14BS, and GC16BS, the architecture of the crystalline phase involved in the C→S transition remains unknown because these were polymorphs that were formed only by heating or grinding of their respective low-temperature crystalline phases, which precluded isolation of single crystals for X-ray structure determination.

The ability of GCnBS compounds to form smectic phases at elevated temperatures prompted us to examine a homologous series of guanidinium alkylbiphenylsulfonates (GCnBPS). These compounds also displayed smectic behavior for alkyl chain lengths $n \geq 7$ (Figure 10). Like GCnBS, the *d*-spacings for the GCnBPS smectic phases increased linearly with *n*, albeit with some scatter compared with GCnBS. ^{1}H NMR suggests this may be due to minor amounts of impurities, most likely unsulfonated biphenylalkanes that are difficult to eliminate during the isolation of the corresponding sulfonates. Extrapolation of the data for both series of compounds to $C = 0$ afforded values of $d_{\mathrm{C}0} = 17.2$ and 20.5 Å for GCnBS and GCnBPS, respectively. These values are not unexpected based on a model in which the alkyl chains do not substantially penetrate the region between the aromatic rings on the opposing **GS** sheet. The difference between these values (3.3 Å) is roughly equivalent to the difference between the lengths of the phenyl and biphenyl groups (4.3 Å). The slope of the GCnBPS data, however, is $m = 2.0$, substantially larger than the slope calculated from the GCnBS data. Although this apparent discrepancy is not completely understood, it may reflect different packing or orientations of the alkyl chains in the two series or an unexpectedly large influence of minor amounts of impurities on the measured *d*-spacing.

The phase behavior of the GCnBS compounds can be summarized by a phase diagram that illustrates the effect of alkyl chain length (*n*) and temperature (Figure 11). The phase space can be divided into different areas based on crystal architecture (CIL, B, and BB), isotropic melt (I), or smectic liquid crystal (S). The various crystal architectures can also be assigned based on their respective interlayer *d*-spacings (Figure 11b). It is apparent from the diagram that the smectic *d*-spacings are independent of their corresponding crystalline phases. Furthermore, it is apparent that the interlayer *d*-spacings of the smectic phases are nearest those of the BB architectures. This suggests that **GS** hydrogen-bond region in the smectic phases adopts a BB-like structure, although it is likely to be somewhat fluxional. The structures of the high-temperature crystalline phases (α and *β*) remain unknown due to difficulty in producing single crystals for structure determination. The IR spectra of these phases, however, clearly indicate full participation of the **G** N−H groups in hydrogen bonding, suggesting the quasihexagonal motif and either the bilayer or CIL structure.

Rheological Properties of Smectic Phases. The X-ray diffraction data indicated that the GCnBS liquid crystals formed smectic phases rather than nematics, signifying the enforcement provided by the **GS** hydrogen-bonding network. This structural enforcement may also be expected to influence the rheological characteristics of the GCnBS smectic phases. Rheology measurements on GC8BS, GC11BS, and GC14BS performed under oscillatory shear at 220 °C revealed that the effect of alkyl chain length on viscosity was negligible. These compounds, however, did exhibit shear thinning, wherein the viscosity decreases as the frequency, or strain rate, increases (Figure 12a). The dependence of the elastic (G') and loss (G'') moduli on frequency was weak, and G' was greater than G'' over the whole frequency range, indicating that the smectic phase of GC8BS responded like a viscoelastic solid to small deformations (<0.5% strain). Similar behavior has been reported for other

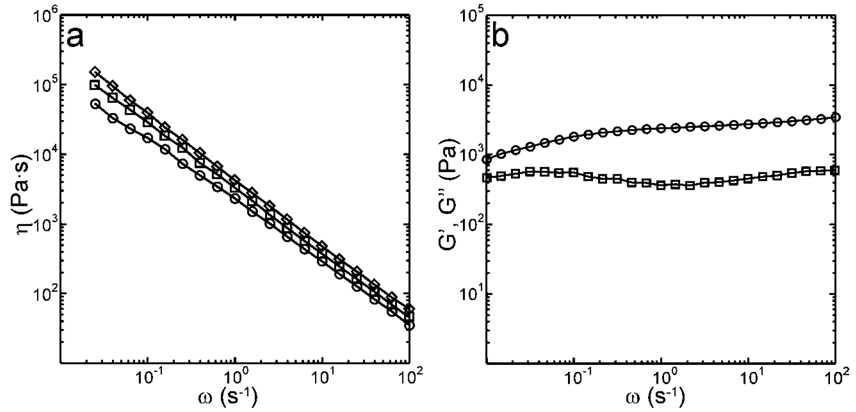

Figure 12. (a) Curves of viscosity vs frequency of GC8BS (○), GC11BS (□), and GC14BS (◇) subjected to oscillatory shear with a strain of $\gamma = 0.3$ at 220 °C. The viscosities display a strong dependence on frequency, indicating shear-thinning behavior. (b) Dynamic (*G*′, ○) and loss (*G*″, □) moduli for GC8BS at 220 °C. *G*′ was greater than *G*″ over the range of frequencies measured, indicating that the smectic phase responds as an elastic solid for small deformations.

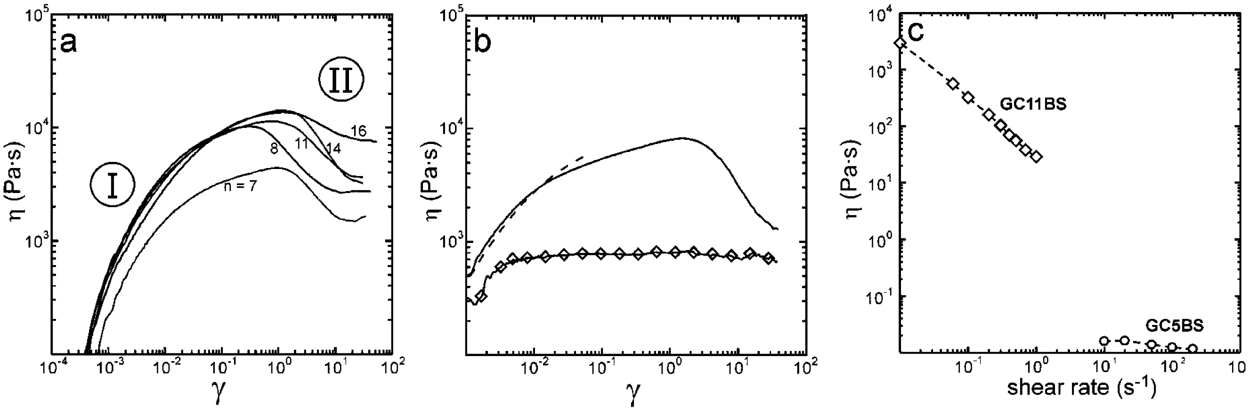

Figure 13. (a) Curves of viscosity (η) vs strain (γ) for GCnBS samples with $n = 7$, 8, 11, 14, and 16 subjected to startup of unidirectional shear at a shear rate of 0.01 s^{-1} at 220 °C. In each case, the viscosity increases with strain (Regime I), undergoes a yielding (depicted schematically in Figure 14), and then approaches a constant value at strains greater than $\gamma \approx 10$ or 1000% (Regime II). (b) Viscosity (η) vs strain (γ) curves for a GC11BS sample subjected to successive shearing at a shear rate of 0.01 s^{-1} at 220 °C. The sample was initially sheared to a strain of $\gamma \approx 0.1$ (dotted line) and then allowed to relax for 10 min. The sample was then sheared past the yield point to a strain of $\gamma \approx 30$ (solid line) and allowed to relax for 10 min. Upon shearing again (◇), there was no sign of yielding, implying that the yielding behavior was irreversible. (c) Viscosities of GC11BS (◇) measured under steady shear after the yield point and viscosities measured for the isotropic melt of GC5BS (○) at 220 °C, plotted with respect to shear rate.

small-molecule smectic phases.[25] The dependence of viscosity on temperature was studied for the GC11BS smectic phase under oscillatory shear, indicating only a weak dependence of the viscosity of the GCnBS smectic phases on temperature in the range 180 °C $\leq T \leq$ 220 °C.

The rheological response of the GCnBS smectic phases to startup of unidirectional shear and continuous shearing at a constant shear rate was examined. These experiments allow an examination of the rheological response at relatively high strains (above $\gamma \approx 10$ strain units or 1000%) and continuous rather than oscillatory shear. Upon startup of unidirectional shearing the smectic phase viscosities exhibited a sharp increase at low strains, followed by a decrease in viscosity between strains of $\gamma \approx 1$ and 10, eventually reaching a plateau at high strains (Figure 13a). Previous work demonstrated that shearing of disordered smectic liquid-crystal phases, such as octylcyanobiphenyl, can produce oriented cylinders or lamella that are characterized by an anisotropic X-ray scattering pattern.[26] Small-angle X-ray scattering measurements of GCnBS smectic phases subjected to shear revealed similar shear-induced ordering of the GCnBS smectic domains. Therefore, the decrease in viscosity at intermediate strains can be attributed to yielding of the sample that accompanied shear-induced ordering of the smectic domains (Figure 14). The maximum value of viscosity attained prior to yielding varied between samples, most likely reflecting different extents of disorder among the samples owing to the vagaries of sample preparation. Small-angle X-ray scattering (SAXS) experiments suggested that the extent of disorder varies significantly in each sample; a randomly oriented sample would display a uniform circular SAXS pattern, while samples with some order exhibited a circular pattern with intensity varying between two maxima. The steady-state viscosity, defined by the plateau after yielding, was $\eta \approx 3 \times 10^3$ Pa·s for GCnBS smectic phases with $n = 8-14$. The GC7BS smectic phase exhibited a slightly lower viscosity over the entire strain range. This may be a signature peculiar

---

[25] Colby, R. H.; Ober, C. K.; Gillmor, J. R.; Connelly, R. W.; Duong, T.; Galli, G.; Laus, M. *Rheol. Acta* **1997**, *36*, 498.

[26] Panizza, P.; Archambault, P.; Roux, D. *J. Phys. II* **1995**, *5*, 303.

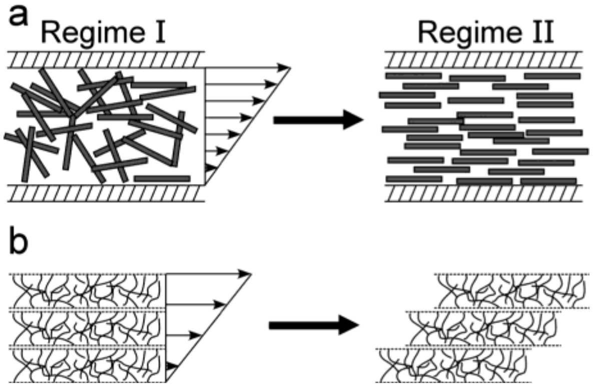

Figure 14. (a) Schematic of the shear-induced alignment of disordered smectic domains that exist prior to yielding (Regime I in Figure 13a) to produce oriented smectic domains (Regime II). (b) Schematic of the flow mechanism of slip between adjacent **GS** sheets.

to a compound that straddles the boundary between isotropic melt and an ordered smectic phase. The GC16BS smectic phase exhibited the highest steady-state viscosity ($\eta \approx 8 \times 10^3$ Pa·s), although it was not significantly larger than the others. The relative insensitivity of the steady-state viscosity on chain length suggests that the principle mechanism of shear-induced flow is slippage between adjacent smectic layers, most likely between adjacent hydrogen-bonded **GS** sheets (Figure 14b). Although the **GS** hydrogen bonding within the GCnBS smectic phases is not as well-defined as in the crystalline state, hydrogen bonding in the smectic phases was confirmed by the FTIR spectra and is corroborated by the rheological behavior. It is likely that slip between smectic layers requires breaking and reforming of hydrogen bonds, which would account for the high viscosities exhibited by the GCnBS smectic liquid crystals.

The occurrence of a yielding signature in the GCnBS smectic phase depended on the rheological history of the sample. For example, if the GC11BS smectic phase was sheared to $\gamma = 0.1$ strain units and then allowed to stand for 10 min without shear, viscosity data for a second shearing (solid line) retraced the first (dotted line) up to a strain of $\gamma = 0.1$ (Figure 13b). This demonstrates that deformation prior to the yield point was elastic and recoverable, the sample relaxing to its original state during the 10 min between the two shearing steps. If the sample was sheared beyond the yield point and then allowed to stand for 10 min without further shear, the yield signature on the next shear cycle disappeared. Instead, the data almost immediately achieved a constant viscosity with a magnitude near that of the plateau observed during the second cycle. These results are consistent with permanent shear-induced ordering of disordered smectic domains at and beyond the yield point, such that the yield signature disappears on subsequent shearing cycles. The yield point could be recovered, however, by lowering the temperature of the sample below $T_{S\rightarrow C}$. and reheating the crystalline material to above $T_{S\rightarrow C}$. This can be explained by the formation of polycrystalline material below $T_{S\rightarrow C}$, which upon heating regenerated disordered smectic domains that once again were susceptible to yield under shear.

The continuous shear steady-state viscosities of the GCnBS smectic phases also reveal significant shear thinning, a behavior characterized by decreasing viscosity with increasing shear rate. The slope of the viscosities of the GCnBS smectic phases plotted with respect to shear rate was ca. −1, as exemplified by GC11BS (Figure 13c), consistent with classical yielding behavior due to plastic deformation.[27] This behavior was similar to that observed for octylcyanobiphenyl (C8BPCN) and other small-molecule smectic liquid crystals.[28] The viscosities measured for the GCnBS smectic phases, however, were at least an order of magnitude larger than those measured for C8BPCN and other small-molecule smectic liquid crystals.[28,29] The high viscosities observed for GCnBS smectic phases can attributed to the infinite hydrogen-bonded **GS** network, which serves to reinforce the smectic structure and increase interactions between adjacent smectic layers.

Conclusion

The structure and phase behavior of molecular materials in both liquid-crystal phases and molecular crystal phases is dependent on several variables, including molecular size, molecular shape, and the magnitude and nature of competing intermolecular interactions. Furthermore, the delicate interplay between different intermolecular interactions often results in complex structural and phase behavior for even the simplest molecular compounds. Through systematic adjustment of the alkyl chain length, this comprehensive examination of the GCnBS and GCnBPS crystalline phases and their smectic counterparts reveals the subtle balance of nondirectional alkyl−alkyl interactions and directional hydrogen bonding.

This balance was revealed by the shift from a $\mathrm{CIL}_{\text{all}-trans}$ architecture to a CIL_{gauche} architecture at $n = 7$, at which the alkyl chains adopt a gauche configuration about the $C_\alpha - C_\beta$ bond, the same chain length that defines the boundary between isotropic melts and smectic liquid-crystal phases. The CIL_{gauche} architecture, in which the chains are oriented parallel to the **GS** sheet, persists through $n = 8-10$, beyond which the alkane chains are sufficiently long to overcome spatial constraints imposed by the **GS** sheet and adopt all-trans chain configurations, with the chains nearly perpendicular to the **GS** sheets. Furthermore, the BB architecture formed by GC12BS, GC14BS, and GC16BS reveals the role of interchain packing forces that become sufficiently dominant to disrupt the otherwise robust hydrogen bonding of the quasihexagonal **GS** network. Nonetheless, these materials retain the layered architecture and **GS** hydrogen bonding upon heating to form stable smectic phases with structures that are independent of the structure of the corresponding crystalline phases, which themselves exhibit different architectures and rich polymorphic behavior. The rheological properties of these smectic phases clearly reveal that hydrogen bonding exerts a significant effect, with yielding behavior and shear thinning that is

---

(27) Macosko, C. W. *Rheology: Principles, Measurements, and Applications*; Wiley-VCH: New York, 1994.

(28) Chapoy, L. L.; Duke, R. W. *Rheol. Acta* **1979**, *18*, 537.

(29) Jadzyn, J.; Dabrowski, R.; Lech, T.; Czechowski, G. *J. Chem. Eng. Data* **2001**, *46*, 110.

qualitatively similar to that of other small-molecule smectics but with viscosities that are 2 orders of magnitude higher.

Experimental Section

Materials. Alkylbenzenes were purchased from Sigma-Aldrich (Milwaukee, WI) and used without further purification. Guanidinium tetrafluoroborate (GBF_4) was prepared by the neutralization of tetrafluoroboric acid with stoichiometric quantities of guanidinium carbonate.

Guanidinium 4′-Alkyl-4-benzenesulfonate (GCnBS). GCnBS compounds were prepared by the direct sulfonation of alkylbenzenes with chlorosulfonic acid. The alkylbenzene was dissolved in a small quantity of chloroform and cooled in an ice bath under a nitrogen atmosphere. A stoichiometric quantity of chlorosulfonic acid ($ClSO_3H$) was added dropwise to the stirred solution, and the solution was stirred for 1 h. The chloroform was removed under reduced pressure, and the resulting alkylbenzenesulfonic acid was dissolved in acetone. An excess of GBF_4 was added to the stirred sulfonic acid solution, resulting in the precipitation of guanidinium 4-alkylbenzenesulfonate in high yield. The resulting white precipitate was filtered and purified by recrystallization in methanol.

Guanidinium 4-Alkylbiphenylsulfonate (GCnBPS). 4-Alkylbiphenyl ketones were prepared according to the previously reported method.[30] The 4-alkylbiphenyl ketones were reduced to 4-alkylbiphenyls by a Wolf–Kischner reduction by the method previously reported for the reduction of 4-*n*-alkanoyl-*p*-terphenyls to 4-alkylterphenyls.[31] The sulfonation of the 4-alkylbiphenyls and the precipitations of the guanidinium salts were performed by the same method described for GCnBS above.

Materials Characterization. Differential scanning calorimetry (DSC) was performed using a Perkin-Elmer Pyris III DSC, with a scan rate of 5 °C/min. All rheological measurements were performed using an ARES II rheometer (Rheometric Science). Oscillatory shear measurements were performed using a 25 mm diameter parallel plate geometry and a strain between 0.3% and 0.5%. Steady shear measurements were performed using a 25 mm diameter cone and plate geometry (0.1 rad, 0.056 mm gap) and shear rates between of 0.01 and 1 s^{-1}. Infrared spectrometry was performed using a Nicolet Magna 550 FT-IR equipped with a Harrick heating stage. Powder X-ray diffraction (XRD) was performed on a Scintag XDS 2002 powder X-ray diffractometer equipped with a hot stage (−100 to 200 °C). Small-angle X-ray diffraction (SAXS) was performed on the 2D-SAXS line at the University of Minnesota Characterization Facility, equipped with a copper rotating anode X-ray source, a Rigaku 2D area detector, a heating stage, and running Bruker SAXS software. SAXS of samples under shear was performed on the 6m-SAXS line at the University of Minnesota Characterization Facility, equipped with a Rigaku Ultrex 18 Kw X-ray generator (copper radiation), a Bruker Hi-Star multiwire area detector, and a Rheometric Scientific Dynamic Mechanical Thermal Analyzer.

Single-Crystal X-ray Structural Analysis. CIF files are included as Supporting Information. Data were collected in the X-ray Crystallographic Laboratory in the Department of Chemistry at the University of Minnesota with a Siemens CCD platform diffractometer with graphite-monochromated Mo Kα radiation ($\lambda = 0.710\,73$ Å) at 173(2) K. The structures were solved by direct methods and refined with full-matrix least-squares/difference Fourier analysis using the SHELX-97 suite of software. All non-hydrogen atoms were refined with anisotropic displacement parameters, and all hydrogen atoms were placed in idealized positions and refined with a riding model. Data were corrected for the effects of adsorption using SADABS. Structural images were created using the X-Seed user interface and POV–RAY.

Acknowledgment. This work was supported by the National Science Foundation (DMR-0305278) and in part by the MRSEC Program of the National Science Foundation under Award Number DMR-0212302. S.M.M. gratefully acknowledges the financial support provided by a Sundahl Fellowship, and the authors thank Victor G. Young, Jr. and the X-ray Crystallographic Laboratory in the Department of Chemistry at the University of Minnesota for assistance with single-crystal X-ray structural analysis and David Walba and Noel Clark (University of Colorado) for helpful discussions.

Supporting Information Available: Crystallographic information files for GCnBS structures ($n = 2, 3, 4, 7, 11, 12, 14, 16$) and GCnBPS structures ($n = 8, 10$). This material is available free of charge via the Internet at http://pubs.acs.org.

CM049594L

---

(30) Long, L. M.; Henze, H. R. *J. Am. Chem. Soc.* **1941**, *63*, 1939.
(31) Sadashiva, B. K.; Subba Rao, G. S. R. *Mol. Cryst. Liq. Cryst.* **1977**, *38*, 345.